Journal of Interfaces, Thin films, and Low dimensional systems 3 (2) Winter and Spring (2020) 251-267

Numerical investigation of a new hybrid system, integrating parabolic trough concentrator with a cylindrical thermoelectric generator

Scientific research paper

Abderrahim Habchi[1*], Bouchaib Hartiti[1], Hicham Labrim[2], Salah Fadili[1], Naoual Belouaggadia[3], Mohammed Benaissa[4], Abdelilah Benyoussef[4], Hamid EZ-Zahraouy[4], Mehmet Ertugrul[5], Esidor Ntsoenzok[6]

[1]*ERDYS Laboratory, MEEM & DD Group, Hassan II University of Casablanca, FSTM BP 146 Mohammedia 20650, Morocco*

[2]*Materials Science Unit / DERS / CNESTEN National Centre for Energy, Sciences and Nuclear Techniques, Rabat, Morocco*

[3]*Laboratory of Signals, Distributed Systems and Artificial Intelligence, ENSET, Hassan II University, Mohammedia, Morocco*

[4]*LAMCSCI, Faculty of Sciences, Mohammed V University, B.P. 1014, Rabat, Morocco*

[5]*Engineering Faculty, Ataturk University, 25240 Erzurum, Turkey*

[6]*CEMHTI-CNRS Site Cyclotron, 3A rue de la Férollerie 45071 Orléans, France*

ARTICLE INFO

Article history:
Received 16 October 2020
Revised 3 January 2021
Accepted 3 January 2021
Available online 20 February 2021

Keywords:
Hybrid parabolic trough
Thermoelectric generator
Power output
Efficiency
Cold/hot mass flow rate

ABSTRACT

Nowadays, exploitation and production of maximum energy from the solar spectrum is a major concern. In the present paper, a numerical study of a new hybrid system consisting of a parabolic trough concentrator coupled with a cylindrical thermoelectric generator is performed using the Gauss-Seidel iterative method. A realistic climatic condition is used regarding direct sunlight and ambient temperature. The effects of thermoelectric generator thickness together with hot and cold flow on the electrical and thermal performance are analyzed and discussed. In order to validate the results of the numerical model, a new validation method has been used. The obtained results show a good agreement with the exact results. Furthermore, for a cold mass flow rate of 0.25 kg/s, the maximum thermal efficiency is attained at 60.646%, along with an electrical efficiency of 9.72% corresponding to 273.15 W in additional to power output.

*Corresponding author.
Email address: isohb2015@gmail.com
DOI: 10.22051/jitl.2021.33504.1047

1 Introduction

The petroleum industry is widely used around the world to produce electrical energy. However, its negative effects on the environment and accumulation of toxic gases (CO_2, N_2O, CH_4 ...) in the atmosphere [1,2] have provoked many investigators to explore on clean and renewable energies which can be used without any negative effects on our planet. According to the statistics provided by the International Renewable Energy Agency (IRENA) in 2019 [3], the production of electrical power from renewable systems has shown a significant development where the overall power produced from solar systems was 8,594 GW, while that from wind was around 622.704 GW (worldwide).

The world production of hydropower and biogas increased significantly from 2010 to 2019, where these renewable systems produced a net power output of 1024.833 GW and 9.518 GW at 2010, respectively, while they increased to 1310.292 GW and 19.453 GW in 2019. The significant power output of renewable systems has stayed low compared to petroleum systems [4]. To this effect, several researches have been carried out to develop renewable systems for producing more power than petroleum systems.

In this context, the interesting renewable systems under consideration are the parabolic trough systems. Thus we have cited only the new developments related to these systems which was achieved by combining standard parabolic trough systems and PV systems with thermoelectric modules [5,6]. Soltani et al [7] developed a tri-generation system by integrating parabolic trough concentrator with PV cells and thermoelectric modules (PV/TEG-PTC). They found that the maximum power output is about 240W with a maximum thermal efficiency of 57%. Also, they have found that the maximum electrical efficiency and power output of TEG are about 0.5% and 2.3W, respectively.

Miljkovic et al. [8] proposed another hybrid parabolic trough configuration which can produce thermal and electrical power by combining parabolic trough collector with TEG characterized by three kinds (Bi_2Te_3, $PbTe_2$ and SiGe). The hybrid parabolic trough concentrator can produce 152 W of electrical power.

Another combination technique changes the geometric design of the collector. Chao Li et al [9] studied the effect of environmental factors (wind speed, solar irradiance, and ambient temperature) on the conversion efficiency of solar thermoelectric co-generation (STECG). They found that the electrical efficiency of STECG increased with increasing sun irradiation, while it decreased with increasing wind speed and ambient temperature. Also, the thermal efficiency of STEGC reduced from 66.66% to 63.28% with increasing sun irradiation. This is due to the increase in heat loss from 19.82% to 23.23%. Similarly, Mahmoudinezhad et al. [10] introduced a new hybrid parabolic trough concentrator integrated with photovoltaic cells and planar thermoelectric modules. They reported that the additional power output of the hybrid parabolic trough concentrator reached 19.13 W. Also, they observed that overall efficiency of the hybrid system was 50.99 %. An experimental/theoretical analysis of a new hybrid solar thermoelectric generator (HSTEG) was introduced by Sundarraj et al [11]. Six thermoelectric generator modules and electrical heaters were integrated inside the parabolic trough collector. The reported maximum thermal and electrical efficiency was about 61% and 1.2%, respectively. The maximum power output was 4.7 W.

In the present study, by the same way as of the previous studies, to improve the electrical and thermal performance of the parabolic trough system, we propose a new combination method. Thus, a new hybrid system, combined parabolic trough concentrator with cylindrical thermoelectric generator has been proposed and analyzed. A 0-D mathematical model is introduced to examine the thermal and electrical efficiencies of the hybrid system, respectively. Seven non-linear thermal equations are solved by the Gauss-Seidel method. This is the first study in which a hybrid parabolic trough system is modeled using two fluids and a cylindrical thermoelectric generator. Also, a novel validation technique has been used to validate our numerical model.

Nomenclature

L	Collector length (m)
l	Collector width (m)
F	Focal distance (m)
ω	Shape factor
α_o	Transmittance − absorptance factor
K	Incident angle modifier
ρ	Surface reflectivity
ρ	Density of glass $\left({}^{kg}/_{m^3}\right)$
C	Specific heat $\left({}^{j}/_{kg.K}\right)$
α	Absorptance factor
D	Diameter (m)
μ	Dynamic viscosity $\left({}^{kg}/_{m.s}\right)$
e	Height (m)
n	Number of thermoelectric modules
S	Seebeck coefficient (V/K)
Δx	Space step (m)
k	Thermal conductivity $\left({}^{W}/_{m.K}\right)$
Δt	Time step (s)
P	Power output (W)
σ	Stefan Boltzmann coefficient$(W/m^2.K^4)$
ε	Emittance
A	Surface area (m^2)
G_d	Sun irradiation (W/m^2)
$\dot{m}$	Mass flow rate (kg/s)
v	Velocity (m/s)
ρr	Electric resistivity $(\Omega.m)$
η_{TEG}	Efficiency of TEG (%)
η_{PTC}	Thermal efficiency of PTC (%)
η_o	Overall efficiency of hybrid PTC (%)

Subscripts

Ab	Absorber
g	Glass
h, hy	Hot, Hydraulic
PTC	Parabolic trough concentrator
HPTC	Hybrid parabolic trough concentrator
TEG	Thermoelectric generator
ou	Outside
in	Inside
max	Maximum
c	Convection
r	Radiation
cd	Conduction
am	Ambiant
f	Fluid
Sim	Simulated
Ref	Reference
cr	Characteristic
TE	Thermoelement
TEGc	Hot side temperature
TEGf	Cold side temperature
hf	Hot fluid
cf	Cold fluid
TAv	Average temperature
T	Temperture

2 System descriptions

According to Fig. 1, the new parabolic trough concentrator configuration is divided into two main parts. The first part is the primary circuit, which consists of the solar reflector (1) and the hybrid collector (2), which includes the glass cover (3), absorber tube (4), tubular thermoelectric generator (5), hot and cold water (6, 7). When the sun radiation is reached at the solar reflector (1), it will be focused directly at the glass cover (3) via the said mirror (1). Thus, a portion of these rays will be partially transmitted to the absorber tube (4). Then, a significant thermal power amount (Thermal energy stored within absorber tube) is absorbed by the hot fluid (Therminol VP[1]) (6) due to the convective heat transfer between the hot fluid (6) and the inner surface of the absorber tube (4). Also, due to the direct contact between the hot fluid (6) and upper side of TEG, the

Table 1. Hybrid system components properties.

Components	Proprieties	Values
[19] PTC	**L**	2×7.8
	l	5
	F	1.84
	$\boldsymbol{\rho}$	0.93
	α_o	0.864
	$\boldsymbol{\omega}$	0.92
	$\boldsymbol{K}$	1
	$\boldsymbol{\alpha_g}$	0.02
	$\boldsymbol{D^{ou}{}_g}$	0.115
	$\boldsymbol{D^{in}{}_g}$	0.109
	$\boldsymbol{C_g}$	1090
	$\boldsymbol{\rho_g}$	2230
	$\boldsymbol{k_g}$	1.2
	$\boldsymbol{D^{ou}{}_{ab}}$	0.070
	$\boldsymbol{D^{in}{}_{ab}}$	0.066
	$\boldsymbol{C_{ab}}$	500
	$\boldsymbol{\rho_{ab}}$	8020
	$\boldsymbol{k_{ab}}$	45
	$\boldsymbol{D_h}$	0.031
	$\boldsymbol{v_{wind}}$	2
	$\boldsymbol{\rho_{hf}}$	850
	$\boldsymbol{C_{hf}}$	$1509 + 2.496 \times T + 788.8 \times 10^{-6} T^2$
	$\boldsymbol{k_{hf}}$	$0.1381 - 0.8708 \times 10^{-4} T - 0.1729 \times 10^{-6} T^2$
	$\boldsymbol{\mu_{hf}}$	$\left(10^{0.8703} \times T^{\left(0.2877 + log\left(T^{-0.3638}\right)\right)}\right) \times 10^{-3}$
	$\boldsymbol{\rho_{cf}}$	$1001.83736 - 0.23291 \times T - 4.95626 \times 10^{-4} \times T^2$
	$\boldsymbol{C_{cf}}$	$4218.2371 - 1.42026 \times T - 0.01378 \times T^2$
	$\boldsymbol{k_{cf}}$	$0.56821 + 1.68 \times 10^{-3} \times T - 5.96341 \times 10^{-6} \times T^2$
	$\boldsymbol{\mu_{cf}}$	$0.00156 - 2.77774 \times T + 1.88979 \times T^2 - 4.28265 \times 10^{-10} \times T^2$
[20] TEG (Bi_2Te_3)	$\boldsymbol{D^{ou}{}_{TEG}}$	0.035
	$\boldsymbol{D^{in}{}_{TEG}}$	0.0292
	$\boldsymbol{k_{TEG}}$	1.548
	$\boldsymbol{\rho_{TEG}}$	8160
	$\boldsymbol{C_{TEG}}$	156
	$\boldsymbol{n}$	780
	$\boldsymbol{L_{TEG}.l_{TEG}.e_{TEG}}$	$40\times40\times4$ $(mm \times mm \times mm)$
	$\boldsymbol{S_p}$,$\boldsymbol{S_n}$	$175 \times 10^{-6}, -175 \times 10^{-6}$
	$\boldsymbol{\rho r_{TEG}}$	0.8×10^{-5}

heating process of the TEG upper side is similar to that of hot fluid which increases the top side temperature of TEG.

In order to create a large temperature difference across the thermoelectric generator, cold water (7) is passed through the inner side of TEG using a regular pump (9). Thus, the cold water (7) is passed along the hybrid collector to the storage tank (12) at 45°C. As a result, the outlet cold water is used to heat the tank's water through a heat exchanger as shown in Fig. 1. Meanwhile, a hot fluid pump (8) is used to circulate the hot fluid (6) from the principal tank (10) to the inlet of the hybrid collector towards the main tank.

During the running time, the temperature of the hot fluid (6) can exceed 100°C, which is sufficient to evaporate the water inside the principal tank (10) by means of a heat exchanger. Thus, the generated steam is used to rotate a turbine (11) at a high pressure (secondary circuit), which produces a significant amount of power which is stored in the power plant. Also, the power output generated by TEG is mainly used for supplying the pumps (8, 9).

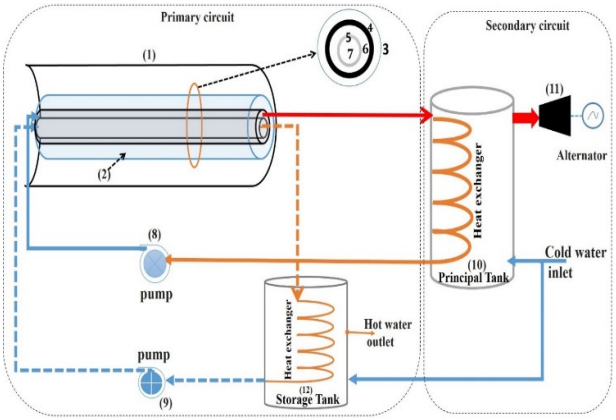

Figure 1. Descriptive diagram of the HPTC system

2.1 Energy balance and calculation process

In order to study the thermal and electrical performance of the HPTC system, a numerical model was used, which based on heat transfer analysis between the heat transfer fluid, absorber tube and the sky.

A cross-sectional view of the HPTC system and thermal coefficients is shown in Fig. 2. From Fig. 2. ${h_{g-am}}^{c}$ and ${h_{g-Sky}}^{r}$ are the convective and radiative exchange coefficients between the upper side of glass cover (3) and the ambient (2) and sky (1), respectively. ${h_{ab-g}}^{c}$ and ${h_{ab-g}}^{r}$ are respectively the coefficients of heat exchange by convective and radiative between the upper side of absorber tube (4) and inner surface of glass cover (3). Also, ${h_{ab-hf}}^{c}$ is the convective exchange coefficient between the inner side of absorber tube (4) and the heat transfer fluid (5). ${h_{TEG-hf}}^{c}$ is the coefficient of heat exchange by convective between the heat transfer fluid (5) and the upper side of TEG (6) while ${h_{TEG-cf}}^{c}$ is the convective exchange coefficient between the inner side of TEG (6) and the cold fluid (7). ${R_{ge-gi}}^{cd}$,${R_{abe-abi}}^{cd}$ and ${R_{TEGe-TEGi}}^{cd}$ are the radial conduction resistances through the glass cover (3), the absorber tube (4) and the cylindrical TEG (6), respectively. The expression for each coefficient of heat exchange is listed in A1-A18.

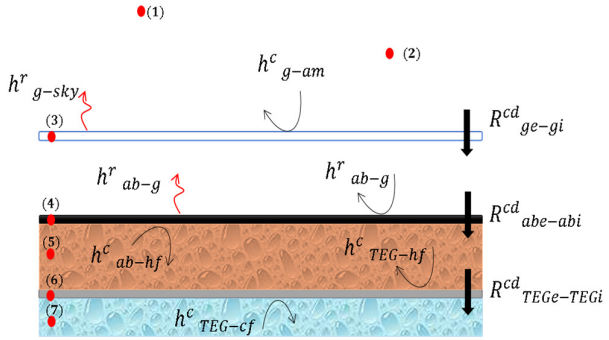

Figure 2. Cross sectional view of the HPTC collector

The thermal and electrical study of all solar systems is mainly based on an energy balance. To this effect, starting from the first thermodynamic law [12], the heat balance equations of the present hybrid system are listed in the following as

- **Glass cover:**

$$\rho_g C_g A_g \frac{dT_g}{dt} = l\rho\alpha_g \omega K G_d + A_g k_g \frac{d^2 T_g}{d^2 x} + \pi D^{ou}{}_{ab} h^c{}_{ab-g}(T_{ab} - T_g) + \pi D^{ou}{}_{ab} h^r{}_{ab-g}(T_{ab} - T_g) - \pi D^{ou}{}_{g} h^c{}_{g-am}(T_g - T_{am}) - \pi D^{ou}{}_{g} h^r{}_{g-sky}(T_g - T_{sky}), \quad (1)$$

- **Absorber:**

$$\rho_{ab} C_{ab} A_{ab} \frac{dT_{ab}}{dt} = l\rho\alpha_o \omega K G_d + A_{ab} k_{ab} \frac{d^2 T_{ab}}{d^2 x} - \pi D^{ou}{}_{ab} h^c{}_{ab-g}(T_{ab} - T_g) + \pi D^{ou}{}_{ab} h^r{}_{ab-g}(T_{ab} - T_g) - \pi D^{ou}{}_{ab} h^r{}_{ab-g}(T_{ab} - T_g) - \pi D^{in}{}_{ab} h^c{}_{ab-hf}(T_{ab} - T_{hf}), \quad (2)$$

- **Hot fluid:**

$$\rho_{hf} C_{hf} A_{hf} \frac{dT_{hf}}{dt} = \pi D^{in}{}_{ab} h^c{}_{ab-hf}(T_{ab} - T_{hf}) + A_{hf} k_{hf} \frac{d^2 T_{hf}}{d^2 x} - \pi D^{ou}{}_{TEG} h^c{}_{hf-TEGh}(T_{hf} - T_{TEGh}) - \dot{m}_{hf} C_{hf} \frac{dT_{hf}}{dx}, \quad (3)$$

- **Hot side of TEG:**

$$\rho_{TEG} C_{TEG} A_{TEG} \frac{dT_{TEGh}}{dt} = \pi D^{ou}{}_{TEG} h^c{}_{hf-TEGh}(T_{hf} - T_{TEGh}) - \frac{T_{TEGh} - T_{Av}}{R_{TEGh}}, \quad (4)$$

- **Cold side of TEG:**

$$\rho_{TEG} C_{TEG} A_{TEG} \frac{dT_{TEGc}}{dt} = \frac{T_{Av} - T_{TEGc}}{R_{TEGc}} - \pi D^{in}{}_{TEG} h^c{}_{TEGc-hf}(T_{TEGc} - T_{cf}), \quad (5)$$

- **Cold fluid:**

$$\rho_{cf} C_{cf} A_{cf} \frac{dT_{cf}}{dt} = A_{cf} k_{cf} \frac{d^2 T_{cf}}{d^2 x} + \pi D^{in}{}_{TEG} h^c{}_{TEGc-cf}(T_{TEGc} - T_{cf}) - \dot{m}_{cf} C_{cf} \frac{dT_{cf}}{dx}. \quad (6)$$

To simulate the six nonlinear equations (1-6), the Gauss-Seidel method is adopted where this technique is based on the finite difference method in order to discretize the six equations by means of schemes of Table 2 and Fig. 3. Meanwhile, the discretized equations are illustrated in Table 3.

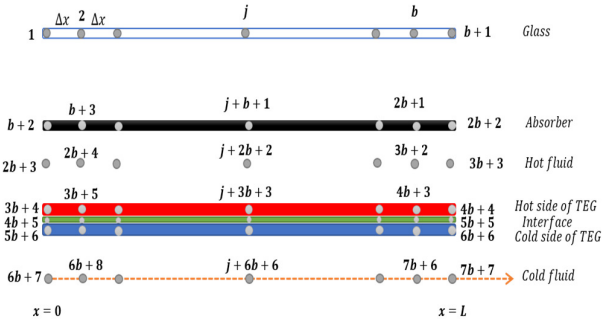

Figure 3. Discretized cross-section of the hybrid collector.

Table 2. Discretization schemes

Discretization schemes / Differential Operators	Schema Centered Left	Centered schema	Schema Centered Right
$\frac{dT_i}{dt}$	**	**	$\frac{T^{t+\Delta t}{}_{i,j} - T^{t}{}_{i,j}}{\Delta t}$
$\frac{d^2T_i}{d^2x}$	**	$\frac{T^{t+\Delta t}{}_{i,j+1} - 2T^{t+\Delta t}{}_{i,j} + T^{t+\Delta t}{}_{i,j-1}}{(\Delta x)^2}$	**
$\frac{dT_i}{dx}$	$\frac{T^{t+\Delta t}{}_{i,j} - T^{t+\Delta t}{}_{i,j-1}}{\Delta x}$	**	**

2.2 Climatic conditions and input parameters

According to Table 3, the set of discretized equations are transformed into a matrix system which is written as [M]{T}={B}. Then the Gauss-Seidel method is used to solve the stated matrix using the boundary conditions shown in Table 3. Moreover, for a faster convergence, a time and space step of 10 sec and 0.2 m have been chosen. The second member {B} contains climatic conditions, namely, the ambient temperature (T_{am}) and sun irradiation(G_d).

In the present work, we have chosen the climatic conditions of Mohammedia [13] (western Morocco) corresponding to 21st December, 2018, as clearly presented in Figs. 4a and 4b.

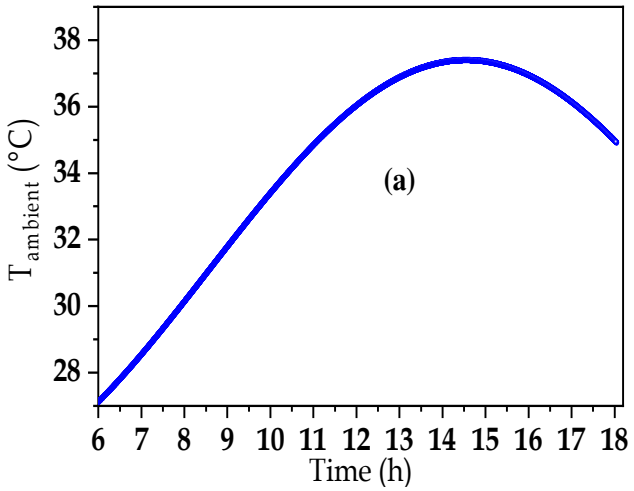

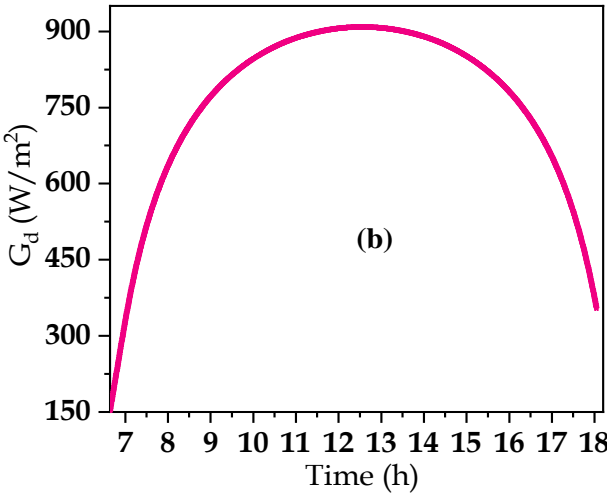

Figure 4. Variation of ambient temperature (panel a) and sun irradiation (panel b) in 21/06/2018.

During the numerical simulation, the following assumptions are considered:

- Uniform repartition of sun irradiation around the absorber tube.
- The heat transfer is considered along one dimension that is z-axis.
- Thermoelectric generator properties are constants.
- Uniform cold fluid mass flow rate.

Table 3. The Discretized equations of the HPTC system

Components	Discretized energy balances	Boundary conditions
Glass cover $2 \le j \le b$	$-\mathbf{A_1}.\mathbf{T^{t+\Delta t}_{j-1}} + \mathbf{B_1}.\mathbf{T^{t+\Delta t}_{j}} - \mathbf{A_1}.\mathbf{T^{t+\Delta t}_{j+1}} - \mathbf{C_1}.\mathbf{T^{t+\Delta t}_{j+(b+1)}} = \mathbf{D_1}$	$\begin{cases} T(t,1) = T(t,2) \\ T(t,b) = T(t,b+1) \end{cases}$
Absorber $b+3 \le j \le 2b+1$	$-\mathbf{A_2}.\mathbf{T^{t+\Delta t}_{j-1}} + \mathbf{B_2}.\mathbf{T^{t+\Delta t}_{j}} - \mathbf{A_2}.\mathbf{T^{t+\Delta t}_{j+1}} - \mathbf{C_1}.\mathbf{T^{t+\Delta t}_{j-(b+1)}}$ $-\mathbf{E_1}.\mathbf{T^{t+\Delta t}_{j+(b+1)}} = \mathbf{D_2}$	$\begin{cases} T(t,b+2) = T(t,b+3) \\ T(t,2b+1) = T(t,2b+2) \end{cases}$
Hot fluid $2b+4 \le j \le 3b+2$	$-\mathbf{A_3}.\mathbf{T^{t+\Delta t}_{j-1}} + \mathbf{B_3}.\mathbf{T^{t+\Delta t}_{j}} - \mathbf{N}.\mathbf{T^{t+\Delta t}_{j+1}} - \mathbf{E_1}.\mathbf{T^{t+\Delta t}_{j-(b+1)}}$ $-\mathbf{F}.\mathbf{T^{t+\Delta t}_{j+(b+1)}} = \mathbf{D_3}$	$\begin{cases} T(t,2b+3) = T(t,2b+4) \\ T(t,3b+2) = T(t,3b+3) \end{cases}$
Hot side of TEG $3b+5 \le j \le 4b+3$	$\mathbf{B_4}.\mathbf{T^{t+\Delta t}_{j}} - \mathbf{A_4}.\mathbf{T^{t+\Delta t}_{j+(b+1)}} - \mathbf{F}.\mathbf{T^{t+\Delta t}_{j-(b+1)}} = \mathbf{D_4}$	$\begin{cases} T(t,3b+4) = T(t,3b+5) \\ T(t,4b+3) = T(t,4b+4) \end{cases}$
TEG interface $4b+6 \le j \le 5b+4$	$\mathbf{2}.\mathbf{T^{t+\Delta t}_{j}} - \mathbf{T^{t+\Delta t}_{j+(b+1)}} - \mathbf{T^{t+\Delta t}_{j-(b+1)}} = \mathbf{0}$	$\begin{cases} T(t,4b+5) = T(t,4b+6) \\ T(t,5b+4) = T(t,5b+5) \end{cases}$
Cold side of TEG $5b+7 \le j \le 6b+5$	$-\mathbf{A_5}.\mathbf{T^{t+\Delta t}_{j-1}} + \mathbf{B_5}.\mathbf{T^{t+\Delta t}_{j}} - \mathbf{A_5}\,\mathbf{T^{t+\Delta t}_{j+1}} - \mathbf{F_2}.\mathbf{T^{t+\Delta t}_{j+(b+1)}} = \mathbf{D_5}$	$\begin{cases} T(t,5b+6) = T(t,5b+7) \\ T(t,6b+5) = T(t,6b+6) \end{cases}$
Cold fluid $6b+8 \le j \le 7b+6$	$\mathbf{B_6}.\mathbf{T^{t+\Delta t}_{j}} - \mathbf{N_2}.\mathbf{T^{t+\Delta t}_{j+1}} - \mathbf{F_2}.\mathbf{T^{t+\Delta t}_{j-(b+1)}} = \mathbf{D_6}$	$\begin{cases} T(t,6b+7) = T(t,6b+8) \\ T(t,7b+6) = T(t,7b+7) \end{cases}$
Coefficients	$A_1 = \frac{A_g k_g}{(\Delta x)^2}\ ;\ B_1 = 2\frac{A_g k_g}{(\Delta x)^2} + \frac{\rho_g A_g C_g}{\Delta t} + \pi D^{ou}{}_{ab} h^c{}_{ab-hf} + \pi D^{ou}{}_g h^{ou}\ ;$ $C_1 = \pi D^{ou}{}_{ab} h^c{}_{ab-hf}$ $D_1 = l\rho\alpha_g \omega K G^d + \frac{\rho_g A_g C_g}{\Delta t} T^t{}_j + \pi D^{ou}{}_g \left(T_{am} h^c{}_{g-am} + T_{sky} h^r{}_{g-sky}\right);$	
	$A_2 = \frac{A_{ab} k_{ab}}{(\Delta x)^2}\ ; B_2 = 2\frac{A_{ab} k_{ab}}{(\Delta x)^2} + \frac{\rho_{ab} A_{ab} C_{ab}}{\Delta t} + \pi D^{ou}{}_{ab} h^c{}_{ab-hf} +$ $\pi D^{in}{}_{ab} h^c{}_{ab-hf}\ ; C_1 = D^{ou}{}_{ab} h^c{}_{ab-hf}\ ;\ E_1 = \pi D^{in}{}_{ab} h^c{}_{ab-hf}\ ;$ $D_2 = l\rho\alpha_o \omega K G^d + \frac{\rho_{ab} A_{ab} C_{ab}}{\Delta t} T^t{}_j\ ;$	
	$A_3 = \frac{A_{hf} k_{hf}}{(\Delta x)^2} + \frac{\dot{m}_{hf} C_{hf}}{\Delta x}\ ;\ F = \pi D^{ou}{}_{TEG} h^c{}_{hf-TEGh}\ ; N = \frac{A_{hf} k_{hf}}{(\Delta x)^2}\ ; D_3 =$ $\frac{\rho_{hf} A_{hf} C_{hf}}{\Delta t} T^t{}_j\ ;\ B_3 = 2\frac{A_{hf} k_{hf}}{(\Delta x)^2} + \frac{\rho_{hf} A_{hf} C_{hf}}{\Delta t} + \frac{\dot{m}_{hf} C_{hf}}{\Delta x} + \pi D^{in}{}_{ab} h^c{}_{ab-hf} +$ $\pi D^{ou}{}_{TEG} h^c{}_{hf-TEGh}\ ;\ E_1 = \pi D^{in}{}_{ab} h^c{}_{ab-hf}\ ;$	
	$B_4 = 2\frac{A_{hT} k_{hT}}{(\Delta x)^2} + \frac{\rho_{hT} A_{hT} C_{hT}}{\Delta t} + \pi D^{ou}{}_{TEG} h^c{}_{hf-TEGh}\ ; D_4 = \frac{\rho_{hT} A_{hT} C_{hT}}{\Delta t} T^t{}_j\ ;$ $F = \pi D^{ou}{}_{TEG} h^c{}_{hf-TEGh}\ ;$	
	$A_5 = \frac{A_{cT} k_{cT}}{(\Delta x)^2}\ ;\ F_2 = \pi D^{in}{}_{TEG} h^c{}_{TEGc-cf}\ ; D_5 = \frac{\rho_{cT} A_{cT} C_{cT}}{\Delta t} T^t{}_j\ ;$ $B_5 = 2\frac{A_{cT} k_{cT}}{(\Delta x)^2} + \frac{\rho_{cT} A_{cT} C_{cT}}{\Delta t} + \pi D^{in}{}_{TEG} h^c{}_{TEGc-cf}\ ;$	
	$N_2 = \frac{A_{cf} k_{cf}}{(\Delta x)^2}\ ; D_6 = \frac{\rho_{cf} A_{cf} C_{cf}}{\Delta t} T^t{}_j\ ; F_2 = \pi D^{in}{}_{TEG} h^c{}_{TEGc-cf}$ $B_6 = 2\frac{A_{cf} k_{cf}}{(\Delta x)^2} + \frac{\rho_{cf} A_{cf} C_{cf}}{\Delta t} + \pi D^{in}{}_{TEG} h^c{}_{TEGc-cf} + \frac{\dot{m}_{cf} C_{cf}}{\Delta x}\ ;$	

3 Results and discussion

3.1 Validation

In this section, the thermal and electrical performance of the HPTC system are presented and discussed. Before that, to validate our numerical model, one of the following methods is performed regarding the numerical model validation:

1. Validation with experimental model.

2. Validation of each subsystem independent from the other.

The first method requires considerable time and investment to be carried out properly. For this reason, we have chosen the second method to validate our numerical model. Based on this method, the parabolic trough system is validated separately for TEG (Isolated TEG). The obtained results are compared with [14]. Then, we validate the obtained results with that of [15].

3.1.1 PTC validation part

During the validation of our simulation program, the same climatic conditions in [14] are respected, also, the same working fluid is used (Therminol VP[1]). Therefore, the temperature distribution of each component of [14] is strongly and roughly similar to that of our simulation as clearly shown in Fig. 5. To prove the validation of our numerical model, two mathematical equations have been used as shown by the following equations

$$\epsilon_{ab} = \frac{\sum_{i=1}^{N}(|y_R - y_S|)}{N}, \quad (7)$$

$$\epsilon_{per} = \frac{\sum_{i=1}^{N}(|y_R - y_S|/y_S)}{N}, \quad (8)$$

where, y_S is the value for the base case, y_R is the deviation from the base value, and N is the number of numerical data.

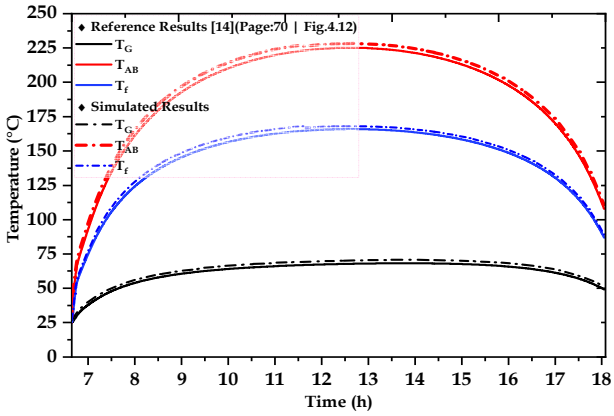

Figure 5. Temperature evolutions of all the PTC's components.

Table 4. Percentage and absolute errors of all the PTC's components.

	Error %	Absolute Error
Glass temperature (°C)	3,62	2,194
Absorber temperature (°C)	2,392	3,514
Fluid temperature (°C)	2,278	2,587

Based on Table 4, the absolute error and its percentage are relatively small, which is acceptable which validate our numerical model.

3.1.2 Cylindrical thermoelectric validation part

In order to compare the obtained numerical results of the TEG with that presented in [15], the same numerical model has been used, keeping all assumptions and conditions applied to the isolated TEG in [15].

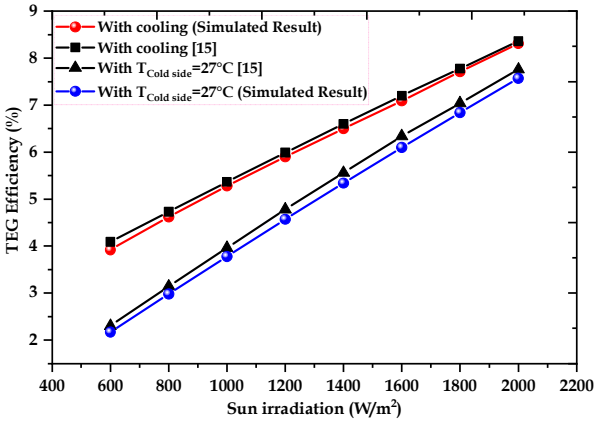

Figure 6. Thermoelectric efficiency of numerical and exact results [15].

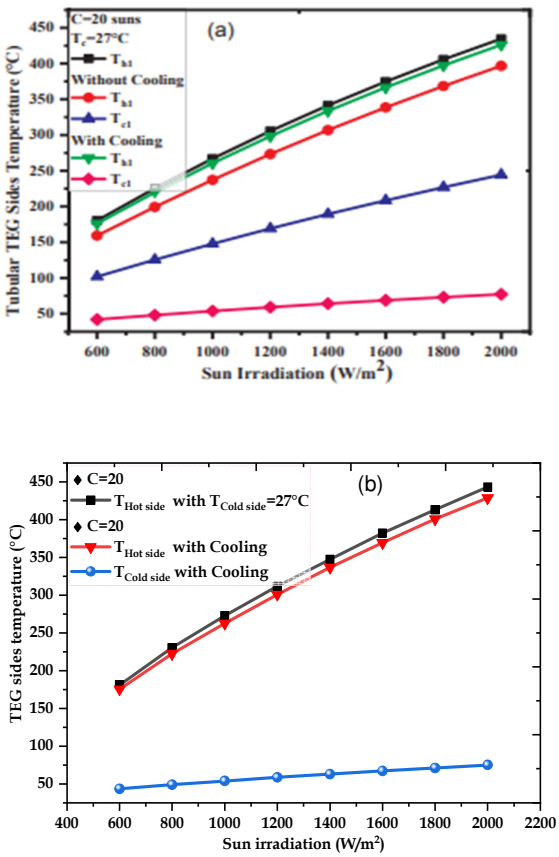

Figure 7. Hot and cold sides temperature of thermoelectric generator of exact (panel a) and numerical results (panel b) [15].

Table 5. Percentage and absolute errors of the TEG sides temperature and efficiency of our numerical model and literature results.

Temperature and efficiency of TEG	Absolute Error	Error %
$T_{cold\ side}$(°C)	1.25	2.063
$T_{hot\ side}$(°C) with cooling system	2.4	0.773
$T_{hot\ side}$(°C) with $T_{cold\ side}$(°C)=27°C	5.61	1.73
η_{TEG} with cooling system	0.0987	1.775
η_{TEG} with $T_{cold\ side}$(°C)=27°C	0.19125	4.275

Figure 6 shows the variation of the TEG's electrical efficiency versus sun irradiation. We can notice that the electrical efficiency increases with increasing of the sun irradiation on both cases (with cooling system and with $T_{cold\ side}$=27°C). Therefore, the numerical and exact solutions have the same tendency where the maximum error percentage is about 4.275%, which validate our numerical model.

The effect of sun irradiation on the hot and cold sides' temperature of TEG are presented in Figs. 7a and 7b. The hot side temperature increases significantly with increasing the sun irradiation, while the cold side temperature increases slightly due to the cooling system effect. When the cold side temperature is set at 27°C, the hot side temperature increases more when using a cooling system. Thus, this performance is similar to that of [15].

To confirm the validity of numerical results, we use Eqs. (7) and (8), where, N is the number of numerical data which is equal to 8. Based on Table 6, in the first case (cooling system case), the absolute error is about 2.4 corresponding to 0.773% in maximum percentage error. Moreover, when $T_{cold\ side}$=27°C, the percentage error can achieve up to 2.063% with an absolute error of 1.25 which validate our numerical model. According to Table 5 and Table 6, the absolute and percentage errors are still reasonable and acceptable, thus, our numerical model is in good agreement with the exact results [14,15].

3.2 Effect of hot fluid flowrate

Figures 8a and 8b show the variation of the HPTC components temperature. As shown in Fig. 8b, when the hot fluid flow rate is increased, the temperature of heat transfer fluid is decreased due to the heating process of the hot fluid within the absorber tube. i.e. the hot fluid heating is decreased with the increase of the hot fluid flow rate, this behaviour is similar to that of [18]. Also, the temperature of the absorber tube is decreased when the hot fluid flow rate increases which is due to an increase of convective heat losses between the absorber tube and hot fluid.

According to Fig. 8a, the hot side temperature of TEG is gradually decreased due to the low thermal amount exchanged between the heat transfer fluid and the TEG's hot side. Also, the temperature difference decreases when the hot fluid flow rate increases. The upper side temperature of TEG decreases with increasing hot flow as seen in Figs. 8a and 8c.

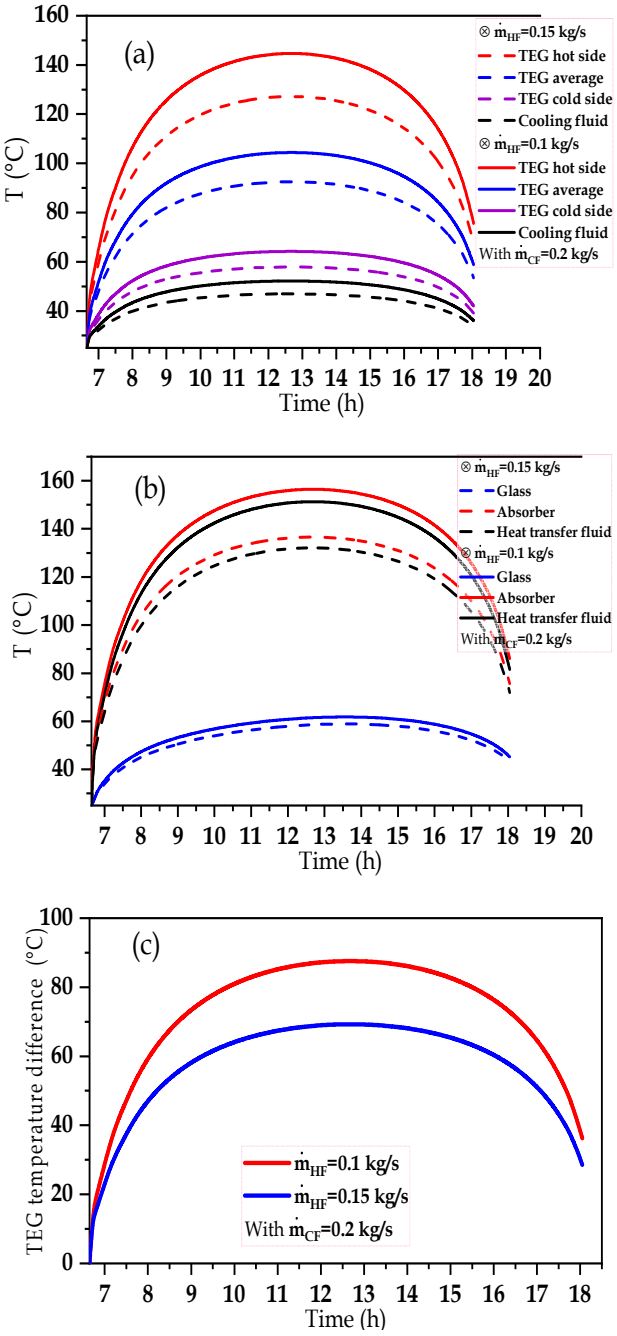

Figure 8. Effect of hot fluid flowrate on the PTC/TEG components temperature distribution (panels (a) and (b)) and the temperature difference of TEG (panel c).

3.3 Effect of cold fluid flow rate

The effect of cold flow rate on the PTC component temperature is shown in the panels of Fig. 9. When the cold fluid flow rate increases, the cold side temperature of TEG decreases significantly as clearly shown in Fig. 9a.

The upper side temperature of TEG and hot fluid temperature decreases due to high cooling effect as seen in Fig. 9b. Thus, the temperature difference across the TEG is increased with increasing the cooling fluid flow rate as shown in Fig. 9c.

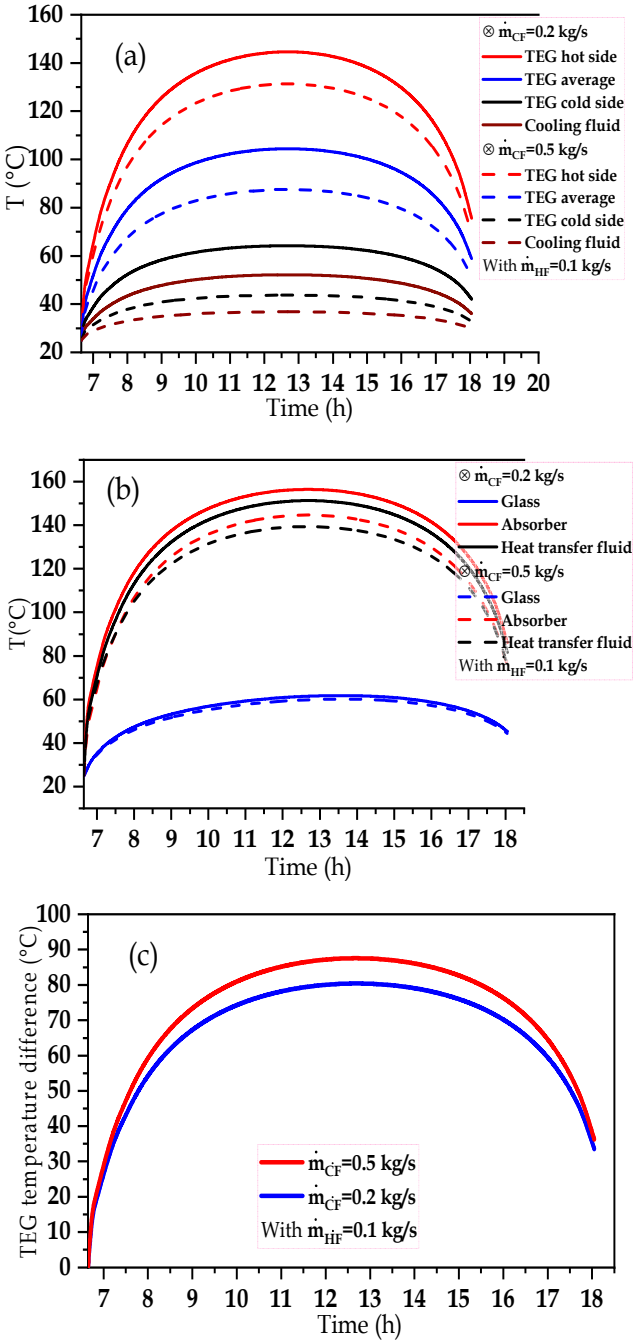

Figure 9. Effect of cold fluid flowrate on the PTC/TEG components temperature distribution (panels a, b) and the temperature difference across the TEG sides (panel c).

3.4 Effect of TEG thickness

The TEG thickness has an important role on the temperature difference variation. Figs.10a and 10b present the temperature of the hot and cold sides at m_{cf}=0.5 kg/s and m_{hf}=0.1 kg/s, while the TEG thickness was varied from 2.9 to 5.8 mm.

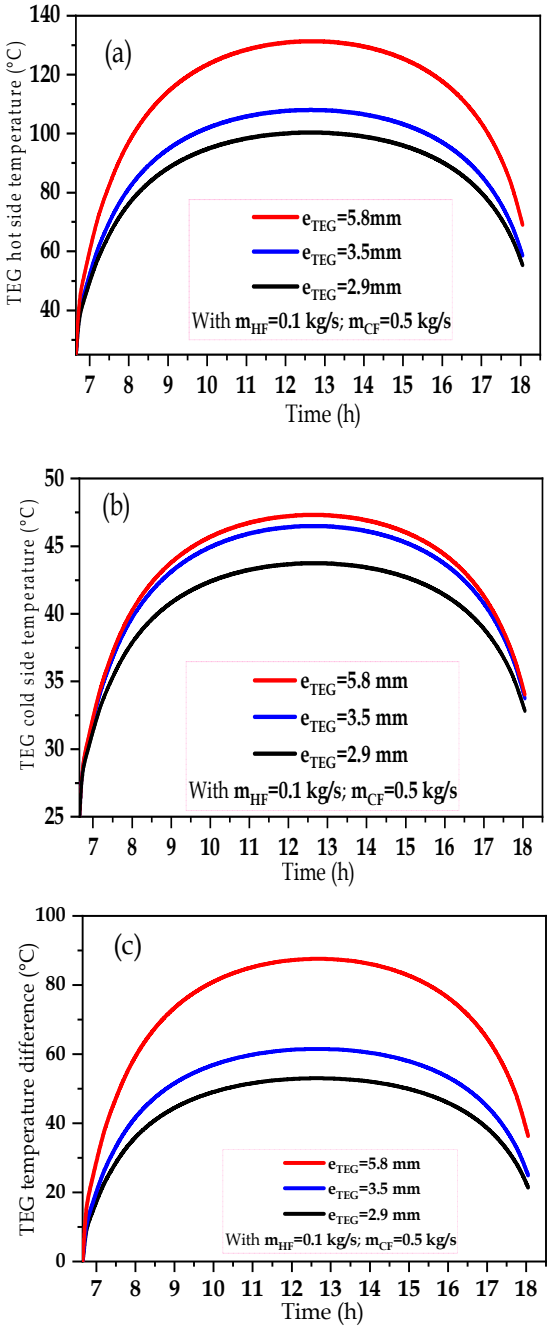

Figure 10. Temperature evolution of hot (panel a) and cold sides (panel b) of the TEG and temperature difference of the TEG (panel c) at different TEG thickness.

It could be noticed that the temperature of hot side of the TEG is increased with increasing TEG thickness, while the cold side temperature is increased slightly when the TEG thickness is increased. This is clearly shown in Figs. 10a and 10b. Therefore, the TEG temperature difference is increased when the TEG thickness is increased which is clearly presented in Fig. 10c.

3.5 Power output and electrical efficiency of TEG

The power output variation of the TEG's is presented in Fig. 11a. It can be noticed that the maximum electrical power increases with increasing the cold fluid flow rate, due to the temperature difference, which is mainly increased with increasing the cold fluid flow rate as explained in subsection 3.3. Also, the power output of the TEG increases with increasing the temperature difference as explained by Eq. (9) and shown in Fig. 11b. Thus, the optimal power output can be reached at m_{cf}=m_{hf}=0.25 kg/s.

$$P_{TEG,max} = \frac{n(S\Delta T)^2}{4R_{in}}. \quad (9)$$

Figure 12 shows the evolution of the TEG's electrical efficiency as a function of sun irradiation. The cold fluid flow rate is varied from 0.25 to 0.4 kg/s with m_{hf} set at 0.25kg/s. Based on Eq. (10), we can notice that the electrical efficiency increases with increasing sun irradiation. This is due to the increases of temperature difference with increasing sun irradiation as explained by [9]. From Figs. 11 and 12, we can also notice that the power output of TEG increases when the electrical efficiency increases due to the strong linear relationship between the electrical efficiency and the power output as explained by Eq. (11). Thus, the maximum electrical efficiency is reached at 9.72% corresponding to 273.15 W in maximum power generation.

$$\eta_{TEG} = \left(\frac{T_{TEGh}-T_{TEGc}}{T_{TEGh}}\right)\frac{\sqrt{1+ZT_{Av}}-1}{\sqrt{1+ZT_{Av}}+\frac{T_{TEGc}}{T_{TEGh}}}, \quad (10)$$

$$P_{TEG} = \eta_{TTEG}(\Delta T)\frac{(1+ZT_{Av})k_{TEG}A^{TEG}}{L_{TEG}}, \quad (11)$$

where, A^{TEG}, k_{TEG}, and Z, L_{TEG} are respectively the cross section of TEG, Thermal conductivity, and merite factor, length of TEG.

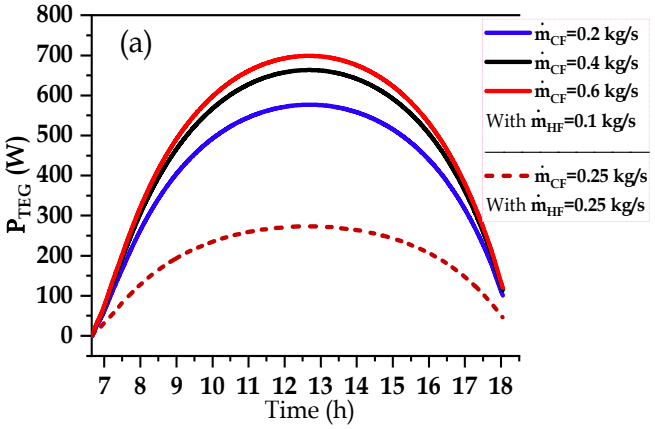

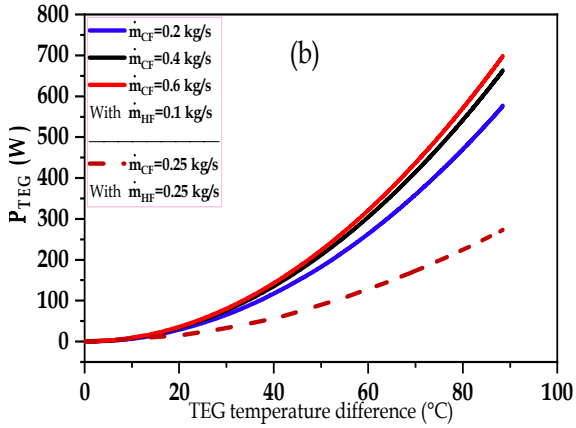

Figure 11. Power output of TEG at various mass flow rate during the whole day (panel a) and for different ΔT (panel b).

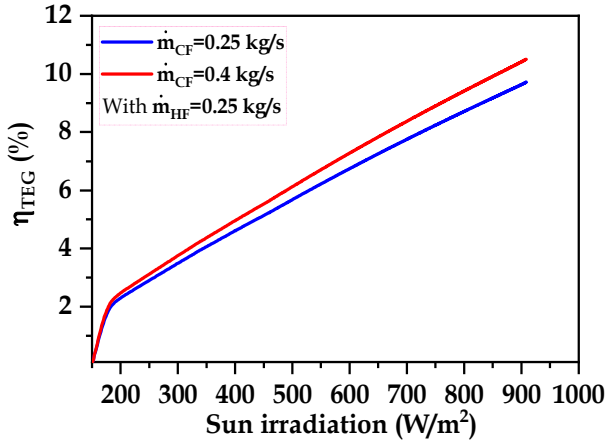

Figure 12. Electrical efficiency of TEG as a function of sun irradiation at different cold fluid flow rates.

3.6 Thermal efficiency of the HPTC system

Figure 13 shows variation of the HPTC's thermal efficiency. The cold fluid flow rate is varied from 0.25-0.4 kg/s with m_{hf}=0.25 kg/s. Based on Eq. (12) [19], it could be noticed that the thermal efficiency (PTC only) decreases slightly with increasing the cold fluid flow rate as shown in Fig. 13. Also, based on Eq. (13) [20], the thermal efficiency of the HPTC system is significantly improved due to integration of the tubular thermoelectric generator inside the PTC system, where the maximum value can be reached at 60.646% corresponding to 273.15 W for the optimal power output of TEG, which is obtained at m_{hf} =0.25 kg/s with m_{hf}=0.25 kg/s.

$$\eta_{PTC} = \frac{\Phi_{th}}{A^{PTC} G_d}, \quad (12)$$

$$\eta_o = \eta_{PTC} + \eta_{TEG}, \quad (13)$$

where, Φ_{th} is the useful thermal power, A^{PTC} is the aperture area, and G_d is the sun irradiation.

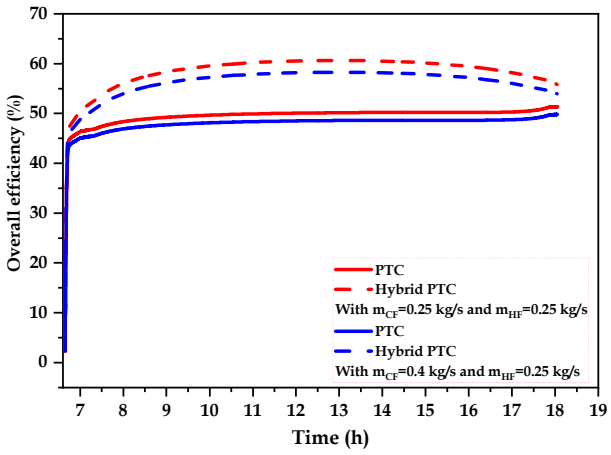

Figure 13. Variation of the HPTC efficiency at different cold fluid flow rates.

4 Conclusions

The thermal and electrical performance of the HPTC system has been investigated. A numerical model was presented while a set of nonlinear equations were solved via the Gauss-Seidel technique. The calculation procures were developed in MATLAB (R2015a) to examine the electrical and thermal performance of the HPTC system. Our major findings are summarized as

- The maximum electrical efficiency is 9.72% corresponding to 273.15 W as elecrical power output.
- The overall thermal efficiency of the HPTC system is about 60.646%, which means that our hybrid system has the ability to generate both thermal and electrical power (additional electrical power) simultaneously, which is very promising for future parabolic trough collector developments.

References

[1] K. Kakaei, M. D. Esrafili, A. Ehsani. "Gas Convertor and Storage." Interface Science and Technology, **27** (2019) 387.

[2] O. Badr, S. D. Probert. "Sinks and environmental impacts for atmospheric carbon monoxide." Applied Energy, **50** (1995) 339.

[3] W. Adrian, R. Sonia, A. Dennis, E. Nazik, E. Gerardo, A. Lana. Renewable Capacity Statistics 2020 n.d. https://www.irena.org/publications/2020/Mar/Renewable-Capacity-Statistics-2020.

[4] M. Daugy. Monthly electricity statistics n.d. https://www.iea.org/reports/monthly-electricity-statistics.

[5] P. Sundarraj, D. Maity, S. S. Roy, R. A. Taylor. "Recent advances in thermoelectric materials and solar thermoelectric generators – a critical review." RSC Advances, **4** (2014) 46860.

[6] A. Z. Sahin, K. G. Ismaila, B. S. Yilbas, A. Al-Sharafi. "A review on the performance of photovoltaic/thermoelectric hybrid generators." International Journal of Energy Research, **44** (2020) 3365.

[7] S. Soltani, A. Kasaeian, T. Sokhansefat, M. B. Shafii. "Performance investigation of a hybrid photovoltaic/thermoelectric system integrated with parabolic trough collector." Energy Conversion and Management, **159** (2018) 371.

[8] N. Miljkovic, E. N. Wang. "Modeling and optimization of hybrid solar thermoelectric systems with thermosyphons." Solar Energy **85** (2011) 2843.

[9] C. Li, M. Zhang, L. Miao, J. Zhou, Y. P. Kang, C. A. J. Fisher et al. "Effects of environmental factors on the conversion efficiency of solar thermoelectric co-generators comprising parabola trough collectors and thermoelectric modules without evacuated tubular collector." Energy Conversion and Management, **86** (2014) 86.

[10] S. Mahmoudinezhad, A. Rezania, L. A. Rosendahl. "Behavior of hybrid concentrated photovoltaic-thermoelectric generator under variable solar radiation." Energy Conversion and Management **164** (2018) 443.

[11] P. Sundarraj, S. S. Roy, R. A. Taylor, D. Maity. "Performance analysis of a hybrid solar thermoelectric generator." Energy Sources, Part A: Recovery, Utilization, and Environmental Effects, **38** (2016) 2977.

[12] A. M. Saleh, Jr DWM, H. I. Abu-Mulaweh. "Flat-Plate Solar Collector in Transient Operation: Modeling and Measurements" 2013.

[13] A. Elamim, B. Hartiti, A. Haibaoui, A. Lfakir, P. Thevenin. "Analysis and comparison of different PV technologies for determining the optimal PV panels- A case study in Mohammedia, Morocco." IOSR JEEE, **12** (2017) 37.

[14] Y. Marif. "Caractérisation d'un concentrateur cylindroparabolique de dimensions réelles au sud de l'Algérie: Région d'Ouargla 2015." http://docplayer.fr/79503677-Caracterisation-d-un-concentrateur-cylindroparabolique-de-dimensions-reelles-au-sud-de-l-algerie-region-d-ouargla.html.

[15] A. Faddouli, H. Labrim, S. Fadili , B. Hartiti, A. Habchi, M. Ertugrul, et al. "Feasibility and performance investigation of a new smart system integrating planar/tubular thermoelectric generators

with solar flat plate collector." Energy Conversion and Management, **199** (2019) 111980.

[16] Y. Marif, H. Benmoussa, H. Bouguettaia, M. M. Belhadj, M. Zerrouki. "Numerical simulation of solar parabolic trough collector performance in the Algeria Saharan region." Energy Conversion and Management, **85** (2014) 521.

[17] Y. Marif. "Caractérisation d'un concentrateur cylindroparabolique de dimensions réelles au sud de l'Algérie: Région d'Ouargla." Thesis. Kasdi Merbah Ouargla, 2015.

[18] F. Jamadi. "Experimantal investigation of effect of oil mass flow changes on parabolic trough collector efficiency in a solar water heater system." International Journal on Technical and Physical Problems of Engineering, **8** (2016) 7.

[19] J. A. Duffie, W. A. Beckman. Solar Engineering of Thermal Processes n.d.:928.

[20] M. Mohsenzadeh, M. B. Shafii, H. Jafari mosleh. "A novel concentrating photovoltaic/thermal solar system combined with thermoelectric module in an integrated design." Renewable Energy **113** (2017) 822.

[21] A. Akbari, E. Mohammadian, S. A. Alavi Fazel, M. Shanbedi, M. Bahreini, M. Heidari, et al. "Natural Convection from the Outside Surface of an Inclined Cylinder in Pure Liquids at Low Flux." ACS Omega, **4** (2019) 7038.

[22] Yunus A çengel. Heat and Mass Transfer: A practical Approach. Third edition. 2006.

[23] G. A. Quadir, I. A. Badruddin, N. J. Salman Ahmed. "Numerical investigation of the performance of a triple concentric pipe heat exchanger." International Journal of Heat and Mass Transfer **75** (2014) 165.

[24] Frank P. Incropera, David P. DeWitt, Theodore L. Bergman, Adrienne S. Lavine. Fundamentals of Heat and Mass Transfer, Sixth Edition 2007.

Appendix

1. Heat transfer coefficients

1.1 Convection between glass cover and ambient

The convective heat transfer coefficient between the glass cover and ambient can take two expressions according to the wind speed value. Thus, when it has a low value, Churchill and Chu [21] proposed the following expression:

$$h_{g-am}{}^{C} = \frac{k_{air}}{D^{ou}{}_{g}}\left[0.6 + 0.387 * \left\{\frac{Ra_{air}}{\left(1+\left(\frac{0.559}{Pr_{air}}\right)^{\frac{9}{16}}\right)^{\frac{16}{9}}}\right\}^{\frac{1}{6}}\right]^{2}, \quad (A.1)$$

where, air properties are calculated at $\frac{T_g+T_{am}}{2}$, in which**:**

$$Pr_{air} = \frac{C_p{}^{air}\,\mu_{air}}{k_{air}}, \quad (A.2)$$

and,

$$Ra_{air} = \frac{2.(T_g-T_{am}).g.C_p{}^{air}.(\rho_{air}{}^{2}).\left(D^{ou}{}_{g}{}^{3}\right)}{k_{air}.\mu_{air}.(T_g+T_{am})}. \quad (A.3)$$

When the wind velocity takes high value, Zukauskas [22] established a new correlation as follows:

$$h_{g-am}{}^{C} = C(Re^{m}{}_{air})(Pr^{n}{}_{air})\left(\frac{Pr_{air}}{Pr_g}\right)^{\frac{1}{4}} * \frac{k_{air}}{D^{ou}{}_{g}}. \quad (A.4)$$

The air properties are calculated at the ambient temperature T_{am} , except Pr_g that is calculated at the glass cover temperature T_g. Where, *C, m, n,* takes values depending on the Reynolds and Prandtl numbers of the air as explained in [22].

1.2 Radiation between glass cover and the sky

The exchanged heat flux by radiation between the glass cover and sky can be written by[19]:

$$\Phi^{r}{}_{g-ciel} = h_{g-Sky}{}^{r} A^{ou}{}_{g}\left(T_g - T_{sky}\right) = \sigma\varepsilon_g A^{ou}{}_{g}\left(T^4{}_{g} - T^4{}_{sky}\right). \quad (A.5)$$

The heat transfer coefficient by radiation can be extracted from the previous relation [19];

$$h_{g-Sky}{}^{r} = \sigma\varepsilon_g\left(T^2{}_{g} + T^2{}_{sky}\right)\left(T_g + T_{sky}\right). \quad (A.6)$$

1.3 Convection coefficient between absorber tube and glass cover

The convection coefficient expression is written as follows [22] :

$$h_{ab-g}{}^{C} = \frac{2K_{eff}}{D^{ou}{}_{ab} log\left(\frac{D^{in}{}_{ab}}{D^{ou}{}_{g}}\right)}, \quad (A.7)$$

where K_{eff} is the effective thermal conductivity, which takes the following expression:

$$K_{eff} = 0.386 * k_{air} * \left(\frac{Pr_{air}}{0.861 + Pr_{air}}\right)^{\frac{1}{4}} * \left(Ra_L\right)^{\frac{1}{4}}. \quad (A.8)$$

The Rayleigh number Ra_L is evaluated at $L_c = \frac{D^{in}{}_{g} - D^{ou}{}_{ab}}{2}$ as explained by [22]:

$$Ra_L = \frac{\left(ln\left(\frac{D^{in}{}_{g}}{D^{ou}{}_{ab}}\right)\right)^4}{\left(L_c{}^3\right)\left(\left(D^{in}{}_{g}\right)^{\frac{-3}{5}} + \left(D^{ou}{}_{ab}\right)^{\frac{-3}{5}}\right)} * \left(Gr_{air} Pr_{air}\right) \quad (A.9)$$

1.4 Radiation coefficient between the absorber tube and glass cover

The radiative heat exchange between the outer surface of absorber tube and inner side of glass cover given by the following equation [19]:

$$h_{ab-g}{}^{r} = \frac{\sigma\left(T^2{}_{g} + T^2{}_{ab}\right)\left(T_g + T_{ab}\right)}{\frac{1}{\varepsilon_{ab}} + \left(\frac{1}{\varepsilon_g} - 1\right)\frac{D^{ou}{}_{ab}}{D^{in}{}_{g}}}. \quad (A.10)$$

1.5 Convection coefficient at the inner side of the absorber and TEG hot side

The convective heat transfer between the heat transfer fluid and absorber tube is given by [23]:

$$\Phi^{c}{}_{ab-hf} = \pi D^{in}{}_{ab} h^{c}{}_{ab-hf}\left(T_{ab} - T_{hf}\right), \quad (A.11)$$

$$\Phi^{c}{}_{hf-TEGh} = \pi D^{ou}{}_{TEG} h^{c}{}_{hf-TEGh}\left(T_{hf} - T_{TEGh}\right), \quad (A.12)$$

where:

$$h^{c}{}_{ab-hf} = h^{c}{}_{hf-TEGh} = \frac{0.023\left(Re^{0.8}\right)\left(Pr^{n}\right) * k_{hf}}{D_h}, \quad (A.13)$$

and, $D_h = \left(D^{in}{}_{ab} - D^{ou}{}_{TEG}\right)$,

in which: Re, Pr and k_{hf} are respectively Reynold and Prandtl number and thermal conductivity of hot fluid, with 'n' takes two values 0.4 and 0.3 for heating and cooling process, respectively.

1.6 Convection coefficient between the inner surface of TEG and the cold fluid

The expression of $\left(h_{TEG-cf}{}^{c}\right)$ is given by [24], where $Re < 2300$, the expression of $Nu_{TEG-cf}{}^{c}$ can be written as:

$$Nu_{TEG-cf}{}^{c} = 4.36. \quad (A.14)$$

If $3000 \leq Re \leq 5.10^6$, the Nusselt number is [24]:

$$Nu_{TEG-cf}{}^{c} = \frac{\left(\frac{f}{8}\right)(Re - 1000)Pr}{1 + 12.7\left(\sqrt{\frac{f}{8}}\right)\left(Pr^{\frac{2}{3}} - 1\right)}, \quad (A.15)$$

with;

$$f = (1.8log_{10}(Re) - 1.5)^{-2}. \quad \text{(A.16)}$$

The final expression of ${h_{TEG-cf}}^{c}$ in both cases is:

$${h_{TEG-cf}}^{c} = \frac{{Nu_{TEG-cf}}^{c}\, k_f}{{D^{in}}_{TEG}}. \quad \text{(A.17)}$$

1.7 Thermal conduction coefficients

The thermal conduction resistance is [24]:

$${R^{cd}}_{n} = \frac{log\left(\frac{r_{ou}}{r_{in}}\right),}{2\pi k_n L} \quad \text{(A.18)}$$

where; k, r_{ou} and r_{in} is the thermal conductivity, outer and inner radius of absorber tube. In which, n: glass cover, absorber and TEG.